ORIGINAL PAPER

Formation and dielectric properties of anodic oxide films on Zr–Al alloys

Shun Koyama · Yoshitaka Aoki · Shinji Nagata · Hiroki Habazaki

Abstract Zr–Al alloys containing up to 26 at.% aluminum, prepared by magnetron sputtering, have been anodized in 0.1 mol dm^{-3} ammonium pentaborate electrolyte, and the structure and dielectric properties of the resultant anodic oxide films have been examined by grazing incidence X-ray diffraction, transmission electron microscopy, Rutherford backscattering spectroscopy, and AC impedance spectroscopy. The anodic oxide film formed on zirconium consists of monoclinic and tetragonal ZrO_2 with the former being a major phase. Two-layered anodic oxide films, comprising an outer thin amorphous layer and an inner main layer of crystalline tetragonal ZrO_2 phase, are formed on the Zr–Al alloys containing 5 to 16 at.% aluminum. Further increase in the aluminum content to 26 at.% results in the formation of amorphous oxide layer throughout the thickness. The anodic oxide films become thin with increasing aluminum content, while the relative permittivity of anodic oxide shows a maximum at the aluminum content of 11 at.%. Due to major contribution of permittivity enhancement, the maximum capacitance of the anodic oxide films is obtained on the Zr–11 at.% Al alloy, being 1.7 times than on zirconium at the formation voltage of 100 V.

Keywords Anodic oxide · Anodizing · Crystalline ZrO_2 · Dielectric oxide · Capacitor

S. Koyama · Y. Aoki · H. Habazaki (✉)
Division of Materials Chemistry, Faculty of Engineering,
Hokkaido University,
Sapporo 060-8628, Japan
e-mail: habazaki@eng.hokudai.ac.jp

S. Nagata
Institute for Materials Research, Tohoku University,
Sendai 980-8577, Japan

Introduction

Anodizing is an important surface treatment method for light metals, and recently has attracted much attention for the fabrication of self-organized nanostructures, including oxide nanohole array, nanotube array, and nanofibers, with many useful properties. Extensive fundamental and application-oriented studies have been so far carried out on anodizing of a range of valve metals.

Growth mechanism of anodic oxide films is dependent upon whether the oxides are amorphous or crystalline. Amorphous anodic oxides, usually formed on aluminum, niobium, tantalum, and tungsten, grow simultaneously both at the metal/film and film/electrolyte interfaces by counter migrations of anion inwards and cations outwards in a cooperative manner under the high electric field [1, 2]. A "liquid droplet" model has been proposed to explain the complex ionic transport in growing anodic oxide films [3], although the quantitative model is still awaited for further precise understanding of the growth process. In contrast, crystalline anodic oxides, formed on zirconium and hafnium, are developed predominantly at the metal/film interface by migration of O^{2-} ions inwards, with little contribution of cation migration. The behavior of titanium during anodizing is slightly different. Titanium forms an amorphous anodic oxide at low formation voltages, but an amorphous-to-crystalline transition occurs above ~5 V [4]. After the transition, the film growth proceeds at reduced efficiency due to oxygen gas generation within growing anodic oxide film [5, 6]. Thus, the films contain always cracks, voids, and blisters.

For the examination of growth mechanism as well as modification of the properties of anodic oxides, foreign species are often incorporated either from electrolyte or from substrate. When the anodic oxides are amorphous, the

growth parameters and film properties, such as transport numbers, field strength, density, and dielectric properties, of anodic oxide films on binary alloys become a compositional average of those on individual metals [7–10]. This means that film properties superior to both anodic oxide films on two individual metals cannot be obtained when the anodic oxides are amorphous. In contrast, it has been realized that capacitances of crystalline anodic oxides on Zr–Ti alloys become higher than those on titanium and zirconium [11]. Recently, we have also found marked enhancement of the capacitance of crystalline anodic ZrO_2 by the incorporation of silicon species, although SiO_2 has low relative permittivity [12]. Thus, foreign species-incorporated anodic ZrO_2 is of interest as a dielectric.

In industry, anodic oxide films have been used as important dielectrics for electrolytic capacitors. Anodic Al_2O_3 and Ta_2O_5 are now widely used, but there is a strong industrial demand in enhancing further capacitance and also in replacing tantalum to other common metals, due to limited natural resources of tantalum.

In this work, the influence of aluminum addition to zirconium on the structure and dielectric properties of anodic oxide films has been examined. Particular attention has been paid on the correlation between the phases of anodic oxide and dielectric properties for the design of ZrO_2-based anodic oxide films with high capacitance.

Experimental

Thin films, approximately 200 nm thick, of zirconium and Zr–Al alloys containing up to 26 at.% aluminum were prepared by DC magnetron sputtering on to flat glass substrates and aluminum substrates. The latter substrates were electropolished at 20 V in a mixture of perchloric acid and ethanol (1:4 volume ratio) below 283 K and subsequently anodized to 200 V at a constant current density of 50 A m^{-2} in 0.1 mol dm^{-3} ammonium pentaborate electrolyte, prior to the sputtering, to provide flat surfaces. The specimens prepared on the aluminum substrates were used mostly for characterization of the anodic oxide films by transmission electron microscope (TEM) and Rutherford backscattering spectroscopy (RBS). The alloy films were sputter-deposited using 99.9% zirconium target of 100 mm in diameter with selected numbers of 99.999% aluminum plates (0.785 cm^2) located symmetrically on the erosion region of the zirconium target. The zirconium target without aluminum plates was used for the preparation of the zirconium films. The aluminum contents in the alloy films were determined using RBS analysis.

The specimens were anodized at several formation voltages up to 100 V for 900 s in stirred 0.1 mol dm^{-3} ammonium pentaborate electrolyte at 298 K, using a two-electrode cell with a platinum counter electrode. Initially, a constant current density of 50 A m^{-2} was applied to reach the selected formation voltage. Electrochemical impedance measurements were carried out in the same electrolyte by applying 50 mV (rms) of sinusoidal alternative voltage in the 10^0 to 10^4 Hz range, and the capacitances of the anodic oxide films were determined by analyzing the Bode diagrams.

Vertical cross-sections of the anodic oxide films were observed using a scanning TEM (Hitachi HD-2000) operating at 200 kV. Electron transparent sections, about 30 nm thick, were generated using an ultramicrotome (Reichert-Nissei Ultracut S) with a diamond knife. The structure of the sputter-deposited zirconium and Zr–Al alloy films, as well as the anodic oxide films, were identified by grazing incidence X-ray diffraction (GIXRD) using Cu Kα radiation with the incident angle of 2º (Rigaku, RINT-2000 system). Compositions of anodic oxide films and alloy films were determined by RBS, using a 2.0-MeV He^{2+} ion beam supplied by a tandem-type accelerator at Tohoku University. The incident ion beam angle was normal to the specimen surface, and the scattered particles were detected at 170º to the incident direction. The measured data were analyzed using the RUMP program. Furthermore, depth profiling analyses of the anodic oxide films were carried out by glow discharge optical emission spectroscopy (GDOES) using a Jobin-Yvon 5000 RF instrument in an argon atmosphere of 850 Pa by applying RF of 13.56 MHz and power of 35 W. Light emissions of characteristic wavelengths were monitored with a sampling time of 0.01 s to obtain depth profiles. The wavelengths of the spectral lines used were 339.198, 396.152, 249.678, and 130.217 nm for zirconium, aluminum, boron and oxygen, respectively. The signals were detected from a circular area of approximately 4 mm diameter.

Results

Phases of deposited alloy films

Figure 1 shows GIXRD patterns of the sputter-deposited zirconium and Zr–Al alloys. The patterns of the Zr–5 and 11 at.% Al alloys reveal an hcp structure, similar to that of zirconium. The Zr–16 at.% Al alloy also shows an hcp structure, but only two diffraction lines of 002 and 103 appear, indicating a grain orientation different from the zirconium and Zr–5 and 11 at.% Al alloy films. The diffraction lines shift slightly to higher angle with an increase in aluminum content with no peaks of any second phase, suggesting dissolution of aluminum in zirconium. The Zr–26 at.% Al alloy film shows only a halo at about 35º, typical of an amorphous structure. Since the equilibrium solubility of aluminum in hcp zirconium is less than 1 at.% below 800 K [13], the present sputter-deposited Zr–
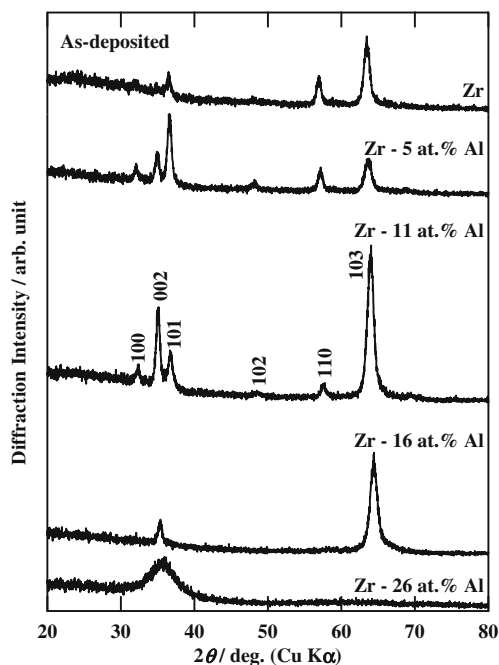
Fig. 1 Grazing incidence X-ray diffraction patterns of the sputter-deposited Zr and Zr–5, 11, 16 and 26 at.% Al alloys

Al alloys are non-equilibrium single-phase solid solutions supersaturated with aluminum. This is in agreement with the fact that sputter-deposited binary alloys often form non-equilibrium single-phase alloys in a wide composition range for a range of binary alloy systems [14].

Voltage–time and current–time curves

Figure 2 shows the voltage–time curves of the zirconium and Zr–Al alloys during initial anodizing at a constant current density of 50 A m^{-2} in 0.1 mol dm^{-3} ammonium pentaborate electrolyte. All specimens show an initial voltage surge of about 2 V, reflecting the presence of a thin air-formed film.
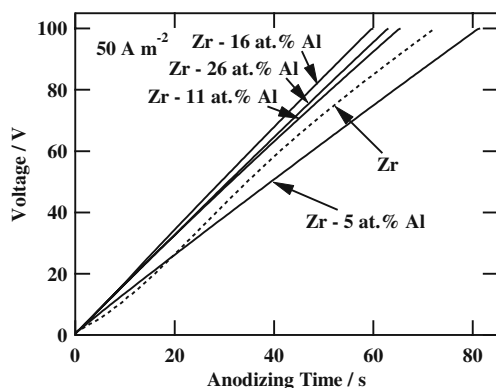

Fig. 2 Voltage–time responses of the sputter-deposited Zr and Zr–Al alloys during initial anodizing at a constant current density of 50 A m^{-2} in 0.1 mol dm^{-3} ammonium pentaborate electrolyte at 298 K

After the surge, the voltages increase approximately linearly with anodizing time. For zirconium, the slope changes at 60 V, probably associated with phase transformation from a high-temperature stable phase (cubic or tetragonal) ZrO$_2$ to monoclinic ZrO$_2$ in the anodic oxide films [11]. The voltages for all Zr–Al alloys increase approximately linearly to 100 V with anodizing time. The slope increases with increase in the aluminum content from 5 to 16 at.% aluminum. The slope for the Zr–26 at.% Al is lower than that for the Zr–16 at.% Al, probably due to structural change as discussed later.

After reaching the selected voltages, anodizing was continued at the respective voltages for 900 s. Figure 3 shows examples of the current transients during anodizing at a constant voltage of 100 V. The currents decrease linearly with anodizing time with a slope of about −1 in the double logarithmic plot for all the specimens. From later RBS analysis, it was found that all the alloys grew anodic oxide films at high current efficiency, but there is nearly four times difference in final current density. The Al–11 at.% Al and Al–26 at.% Al reveal the highest and lowest current densities at anodizing time of 900 s, respectively, although both have a similar slope in the voltage–time curves (Fig. 2).

Transmission electron micrographs

Figure 4 shows transmission electron micrographs of ultra-microtomed sections of the Zr–Al alloy specimens anodized
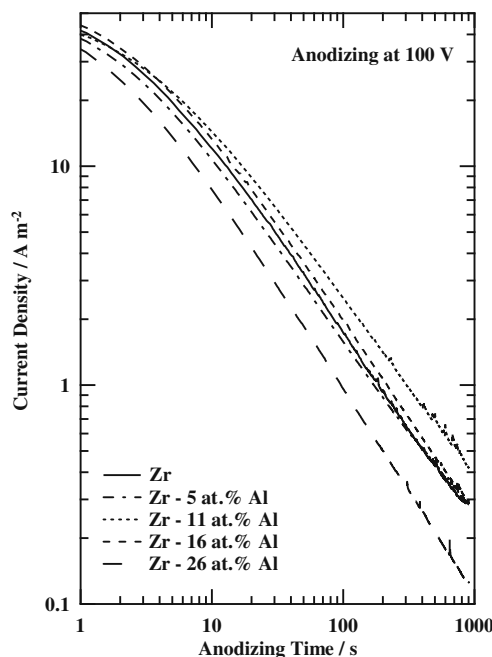

Fig. 3 Current–time curves of the sputter-deposited Zr and Zr–Al alloys during anodizing at 100 V in 0.1 mol dm^{-3} ammonium pentaborate electrolyte at 298 K. Initially, a constant current density of 50 A m^{-2} was applied to reach the selected formation voltage. In this plot, the anodizing time of 0 s was set at the time when the cell voltage reached the selected formation voltage
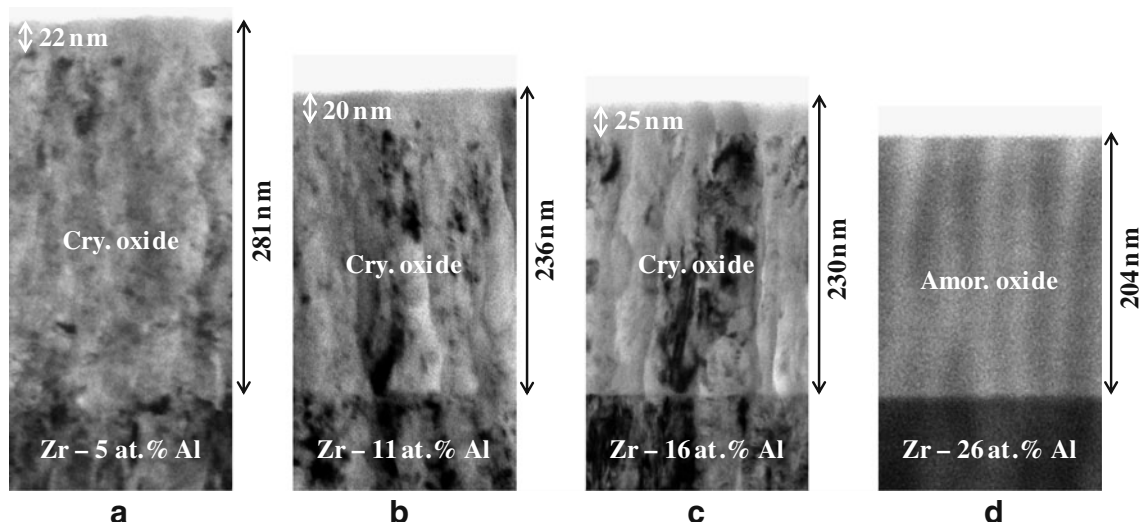
Fig. 4 Transmission electron micrographs of ultramicrotomed vertical cross-sections of the sputter-deposited Zr–5 (**a**), 11 (**b**), 16 (**c**), and 26 at. % (**d**) Al alloys, after anodizing at 100 V in 0.1 mol dm^{-3} ammonium pentaborate electrolyte at 298 K for 900 s, following constant current anodizing at 50 A m^{-2} to the selected formation voltages

at 100 V. Obviously, the anodic oxide films with flat and parallel alloy/film and film/electrolyte interfaces develop on the alloy film, which appears at the bottom of each micrograph. Thinner anodic oxide films are developed with an increase in aluminum content. Thus, the current densities in Fig. 3 appear to be correlated with the thickness of anodic oxide films. Two-layered anodic oxide films, comprising a thin outer amorphous layer and an inner crystalline main layer, are formed on the Zr–5, 11, and 16 at.% Al alloys, with the relative thicknesses of the outer amorphous layer to the total film thickness increasing with aluminum content in alloy, like 7.8%, 8.5%, and 10.9%, respectively. On the other hand, the anodic oxide film on the Zr–26 at.% Al alloy is relatively featureless, and no diffraction contrast is visible throughout the film thickness, indicating that the anodic oxide film is amorphous. The outer ~15 % of the film thickness has slightly light appearance, suggesting the presence of boron species in this region.

Phases in anodic oxide films

Figure 5 shows the GIXRD patterns of the sputter-deposited zirconium and Zr–Al alloy specimens anodized to 100 V. The anodic oxide film formed on the sputter-deposited zirconium at 100 V consists of a mixture of monoclinic ZrO_2 and a high-temperature stable phase ZrO_2, with the former being a major phase, as reported previously [11]. The anodic oxide film formed on the Zr–5 at.% Al alloy also consists of a mixture of monoclinic and high-temperature stable phase ZrO_2, but latter phase becomes more dominant compared with that on zirconium. Furthermore, only a high-temperature stable phase is detected in the GIXRD patterns of the Zr–11 and 16 at.% Al alloy

specimens. No crystalline peaks appear in the GIXRD pattern of the Zr–26 at.% Al alloy specimen, in agreement with the TEM observations. It is difficult to identify from the GIXRD patterns whether the high-temperature phase is cubic or tetragonal because the diffraction patterns for cubic and tetragonal phases are very similar. Raman spectroscopy analysis of the anodized Zr–Si alloys containing up to 16 at. % silicon disclosed that the high-temperature phase was
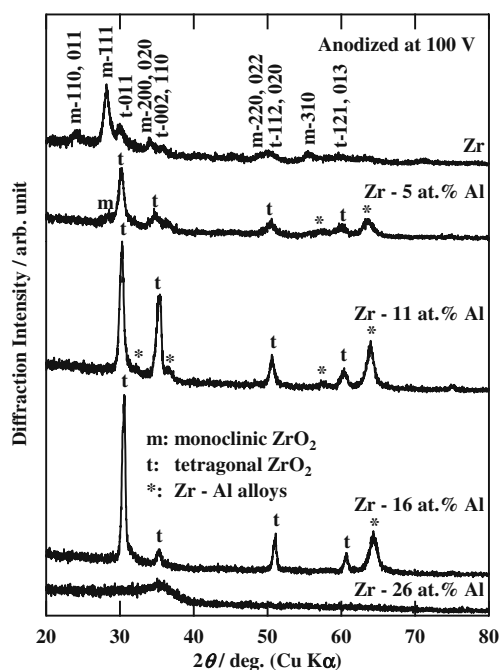

Fig. 5 Grazing incidence X-ray diffraction patterns of the sputter-deposited Zr–Al alloy specimens anodized at 100 V in 0.1 mol dm^{-3} ammonium pentaborate electrolyte at 298 K for 900 s, following constant current anodizing at 50 A m^{-2} to the selected formation voltage

tetragonal, not cubic [15]. Thus, it is also likely that the high-temperature phase in the present anodic oxide films is tetragonal ZrO_2 phase.

GDOES depth profiles

Figure 6 shows the GDOES depth profiles for the Zr–Al alloys anodized at 100 V. The alloy/film interface is located at the sputtering time of 11–15 s, at which sharp rise of intensities of aluminum and zirconium occurs. Both zirconium and aluminum are present throughout the film thickness. The wavy profiles of zirconium and aluminum in the anodic oxide films should be artifact, arising from an optical interference effect caused by transparency of the film for the analyzing wavelength. Boron species, incorporated from the electrolyte, are detected clearly and distribute in the outer part of the anodic films. Assuming a constant sputtering rate throughout the film thickness, the relative thickness of the boron-incorporated region to the total film thickness is 0.12, 0.12, 0.17, and 0.18 for the Zr–5, 11, 16, and 26 at.% Al alloys, respectively.

RBS analysis

The compositions of the anodic oxide films are further analyzed quantitatively using RBS analysis. Figure 7 shows the experimental and simulated spectra for the Zr–Al alloys

anodized at 100 V. The simulated spectra obtained using the thickness, composition, and density, shown in Table 1, fitted well with the experimental spectra. As mentioned above, boron species are incorporated into the anodic oxide films, but boron species are neglected in this simulation because RBS is insensitive to the low concentration of boron. Simulations for all the specimens reveal that the compositions of anodic oxide films are uniform throughout their thickness. Cationic ratios of zirconium and aluminum in the anodic oxide films are in agreement with the alloy compositions. In addition, the charges calculated from the amounts of Zr^{4+} and Al^{3+} ions in the anodic oxide films are close to those passed during anodizing for all the alloy specimens, indicating film growth at high current efficiency (Table 1).

Impedance measurements and dielectric properties

Capacitances of the anodic oxide films formed on the zirconium and Zr–Al alloy films at various formation voltages are determined from electrochemical impedance measurements. Figure 8 shows examples of the Bode diagrams of the specimens anodized at 100 V. All the specimens show the similar behavior of linear change in impedance with a slope close to −1 and phase shift to −90º in the wide frequency region. This behavior is typical of dielectric materials. Similar curves were obtained for

Fig. 6 GDOES depth profiles of the sputter-deposited Zr–5 (**a**), 11 (**b**), 16 (**c**), 26 at.% (**d**) Al alloys anodized at 100 V in 0.1 mol dm^{-3} ammonium penta-borate electrolyte at 298 K for 900 s, following constant current anodizing at 50 A m^{-2} to the selected formation voltage
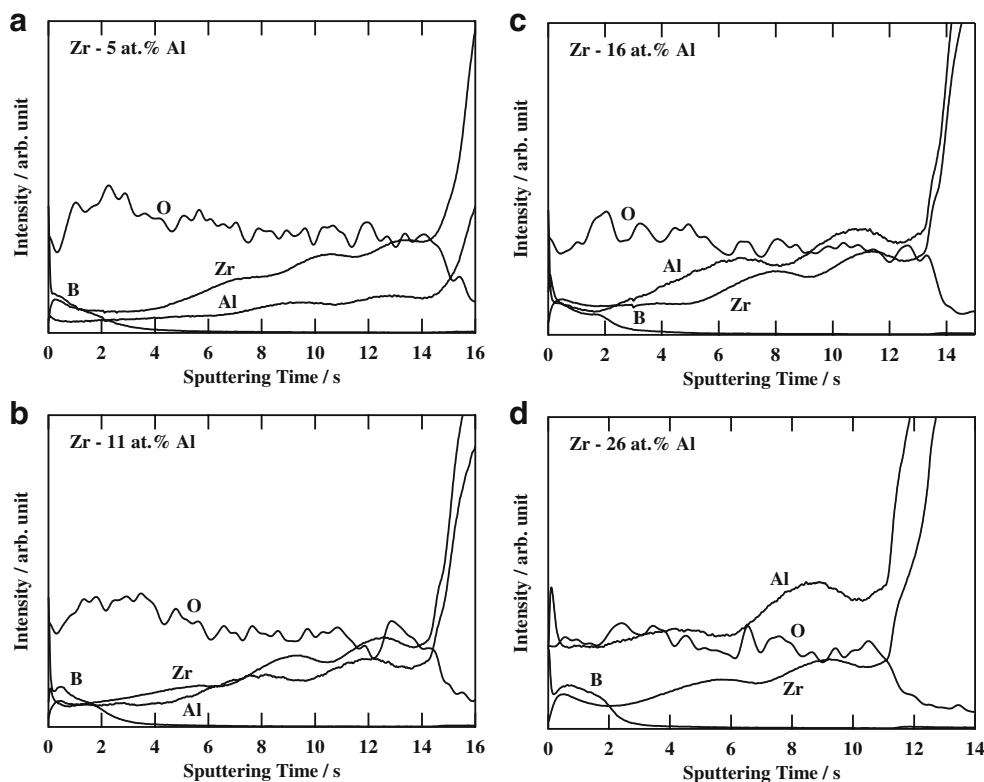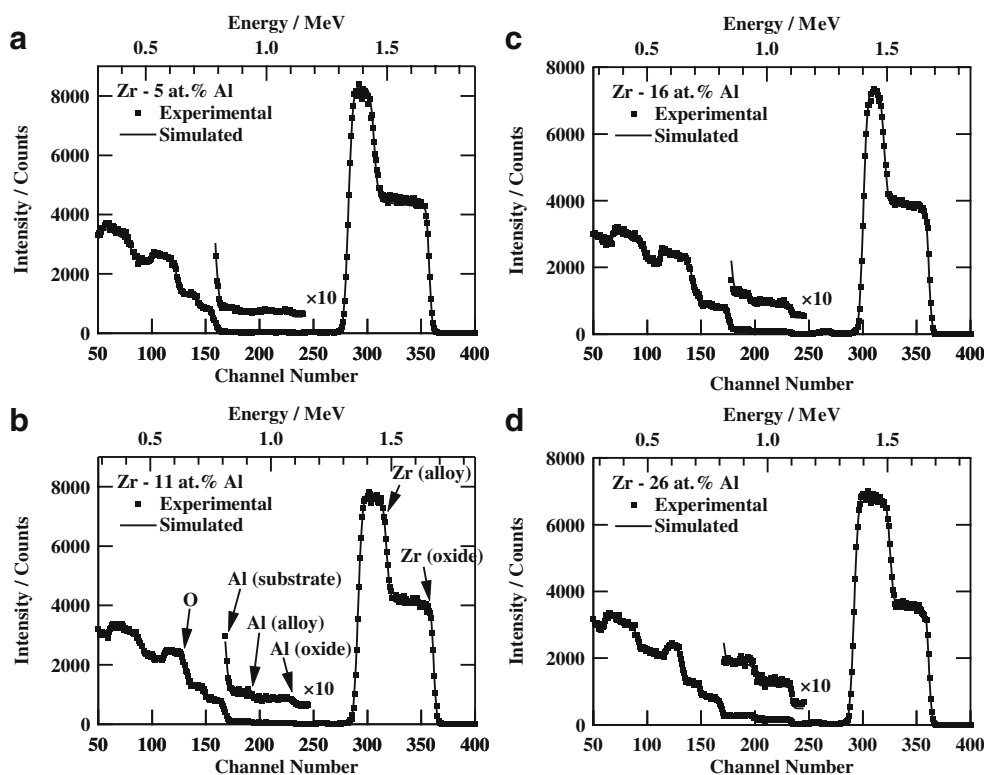
Fig. 7 Experimental and simulated RBS spectra of the sputter-deposited Zr–5 (a), 11 (b), 16 (c), 26 at.% (d) Al alloys anodized at 100 V in 0.1 mol dm^{-3} ammonium pentaborate electrolyte at 298 K for 900 s, following constant current anodizing at 50 A m^{-2} to the selected formation voltage

specimens anodized at other formation voltages. The impedance data were curve fitted using the equivalent electric circuit inserted in Fig. 8. It should be worth mentioning that the anodic oxide films on the Zr–Al alloys containing up to 16 at.% aluminum are two layers with a thin amorphous outer layer. The relative permittivity of the amorphous oxide must be different from the inner crystalline oxide. However, the impedance spectra shown in Fig. 8 show an electrically singe-layer structure. Thus, the impedance spectra were fitted using a single-layer model. The average capacitances of the two-layered anodic oxide films were estimated.

Figure 9 shows the relationship between the film formation voltage and the reciprocal of capacitance of the anodic oxide films on the zirconium and Zr–Al alloy films. The reciprocal capacitances for all the specimens increase linearly with formation voltage, since the capacitance is inversely proportional to the film thickness. Obviously, the capacitances of the anodic oxide films on the Zr–Al alloy films are higher than that on the zirconium film at each formation voltage. The highest capacitance is obtained by the addition of 11 at.% aluminum, with further increase in aluminum content reducing the capacitance.

Discussion

Dielectric properties

In addition to the previously reported silicon addition to zirconium [15], the present study discloses the beneficial effect of aluminum addition in enhancing the capacitance of

Table 1 Results of RBS analysis of the anodic oxide films formed at 100 V on Zr–Al alloys, and current efficiencies of anodizing determined from the ratio of the charges calculated from the amount of cations in the anodic oxide film and the charges passed during anodizing

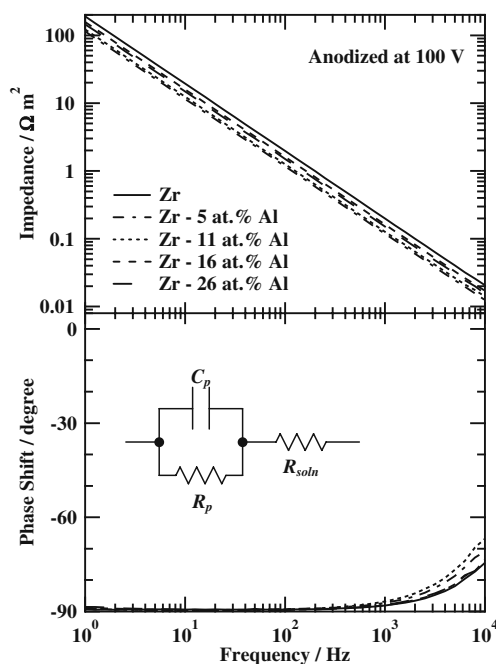| Specimen	Thickness (nm)	Composition*	Density (Mg m^{-3})	Charges calculated (C m^{-2})	Charges passed during anodizing (C m^{-2})	Current efficiency (%)
Zr–5 at.% Al	281	c-$(Zr_{0.95}Al_{0.05})O_{1.98}$	5.39	4,823	4,910	98
Zr–11 at.% Al	236	c-$(Zr_{0.89}Al_{0.11})O_{1.95}$	5.46	4,193	4,344	97
Zr–16 at.% Al	230	c-$(Zr_{0.84}Al_{0.16})O_{1.92}$	5.30	4,045	4,090	99
Zr–26 at.% Al	204	a-$(Zr_{0.74}Al_{0.26})O_{1.87}$	5.12	3,609	3,782	95

*a amorphous, c crystalline

Fig. 8 Impedance Bode diagrams of the sputter-deposited Zr and Zr–Al alloy specimens anodized at 100 V in 0.1 mol dm^{-3} ammonium pentaborate electrolyte at 298 K for 900 s, following constant current anodizing at 50 A m^{-2} to the selected formation voltage

anodic ZrO_2 films. The capacitance of the anodic oxide films on the Zr–11 at.% Al is 1.7 times that on zirconium at 100 V. For a better understanding of the compositional dependence of the capacitance of the anodic oxide films, the capacitance, C, relative permittivity, ε_{ox}, apparent field strength, k^{-1}, of the anodic oxide films formed at 100 V on the present Zr–Al alloys are plotted as a function of alloy composition (Fig. 10). For comparison, the previously reported results of the anodic oxide films on the Zr–Si alloys [15] are also shown in this figure. The maximum capacitances are obtained at ~10 at.% of additive elements for both Zr–Al and Zr–Si alloys. The capacitance per unit area, C, can be expressed by the following equation;

$$C = \varepsilon_0 \, \varepsilon_{ox}/kV$$

where, ε_0 is the permittivity of vacuum, ε_{ox} is relative permittivity, k is formation ratio of anodic oxide film, and V is film formation voltage. It is obvious from this equation that the capacitance at a selected formation voltage can be enhanced by enlarging ε_{ox} and/or reducing k value.

Figure 10b shows the relative permittivities of the anodic oxide films, ε_{ox}, as a function of the content of additive element. The ε_{ox} value of anodic oxide film on zirconium is $\varepsilon_{ox}=23.0$, being in agreement with the values reported previously ($\varepsilon_{ox}=22$–28) [16]. The ε_{ox} values increase to 33–36 when 5–16 at.% of aluminum is added. The Zr–Al

alloys containing 5 to 16 at.% aluminum form crystalline anodic oxides with tetragonal ZrO_2 as a main phase, and the ε_{ox} value of the bulk tetragonal ZrO_2 is also ~35 [17–19]. Thus, the increased ε_{ox} values in these Zr–Al alloys, as well as Zr–5 at.% Si, should be associated with the phase transformation of anodic oxides from monoclinic to tetragonal by the addition of aluminum. Further increase in the additive element content results in the reduction of ε_{ox} value (Zr–26 at.% Al and Zr–10, 16 at.% Si alloys). These anodic oxide films are amorphous or contain amorphous phase. The permittivities of amorphous anodic oxides on binary alloys are compositional average of the anodic oxides formed on the individual metals. Thus, the incorporation of Al_2O_3 ($\varepsilon_{ox}=9.8$) and SiO_2 ($\varepsilon_{ox}=3.5$) units in ZrO_2 results in the decrease in the permittivity.

Figure 10c shows the compositional dependence of reciprocal of formation ratio, k^{-1}. The formation ratio, k, was derived by dividing the film thickness, d, by the film formation voltage, V. The formation ratio for anodic oxide film formed on the Zr–Al alloys decreases moderately with increasing aluminum content in the alloy, due to increase in electric field. On the other hand, the formation ratio for the Zr–Si alloy specimens decreases largely, particularly for Zr–10 and 16 at.% Si alloy specimens. This is attributed to the presence of silicon-rich amorphous phase, which can sustain higher electric field, surrounding nano-grained crystalline oxide in the outer part of anodic oxide film, as reported previously [15].

As seen in Fig. 10a, the maximum capacitance is obtained when 11 at.% of aluminum is added. From the compositional dependence of the ε_{ox} and k^{-1} values (Fig. 10b, c), it is obvious that the capacitance enhancement is mainly attributed to an increase in the ε_{ox} value from 23 to 36. This is in contrast to the Zr–10 at.% Si alloy, in which the major contribution of the capacitance enhancement is the reduction of k value.
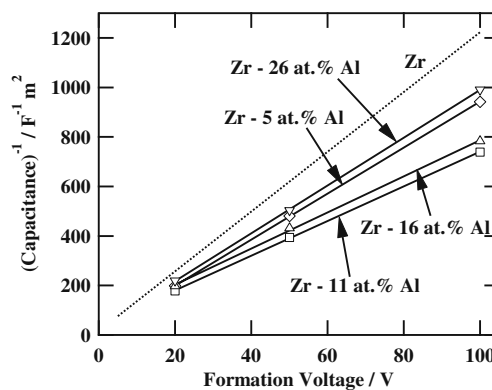

Fig. 9 The formation voltage dependence of the reciprocal of capacitance of the anodic oxide films, formed on the sputter-deposited Zr and Zr–Al alloys in 0.1 mol dm^{-3} ammonium pentaborate electrolyte at 298 K
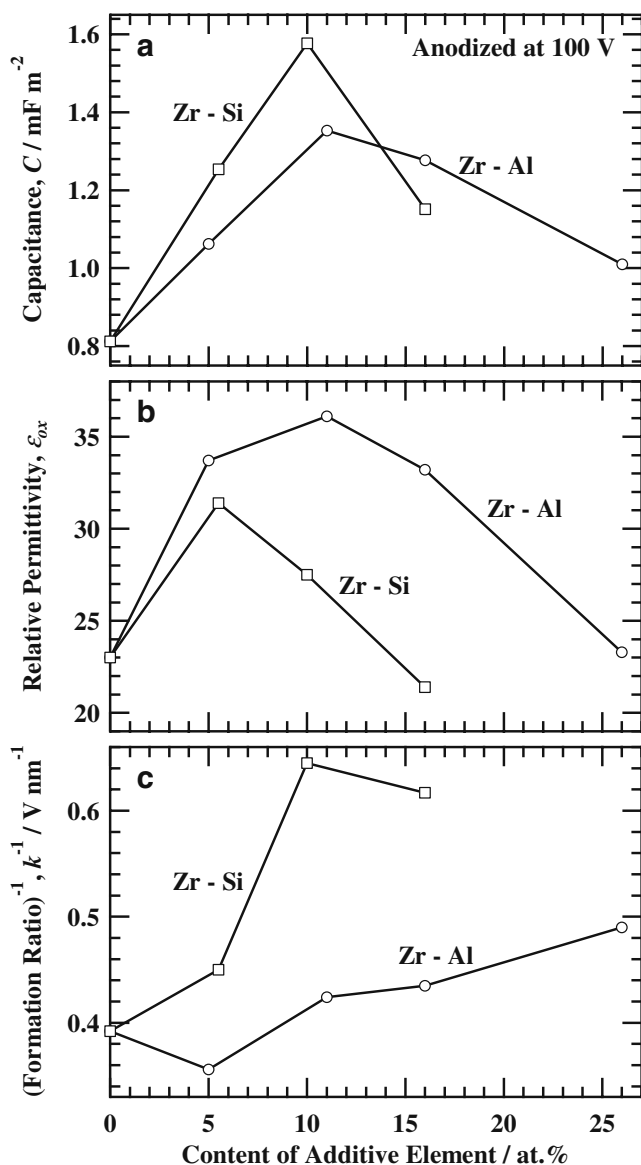
Fig. 10 Capacitance (**a**), permittivity (**b**), and reciprocal (**c**) of formation ratio of the anodic oxide films formed on zirconium and Zr–Al alloys at 100 V, as a function of content of additive element in the alloy. For comparison, data for the anodic oxide films formed on Zr–Si alloys reported previously are shown in the same graphs [15]

Ionic transport in growing anodic oxide films

In the present anodic oxide films formed on the Zr–Al alloys containing up to 16 at.% aluminum, a thin outer layer is amorphous, although inner major part of the anodic oxide films are crystalline. The relative thickness of the outer amorphous layer to the total film thickness increases from 8% for the Zr–5 at.% Al to 11 % for Zr–16 at.% Al alloy. The relative thickness of the outer layer was similar even at low formation voltages. This means that the outer amorphous layer thickens with formation voltage.

It is known that anion transport is predominant in growing crystalline anodic ZrO_2. In this case, it is not possible to grow the outer amorphous layer, since no supply of cations to the outer amorphous layer from the inner crystalline layer. In fact, Zr–5.5 at.% Si form a single crystalline anodic oxide layer, in which silicon species are present throughout the film thickness. Since silicon species are immobile in many anodic oxides [20–24], the result of the Zr–5.5 at.% Si alloy indicates that the anodic oxide film is developed at the alloy/film interface predominantly by the inward migration of O^{2-} ions. The formation and growth of the outer amorphous layer on the Zr–Al alloys must assume the cation transport in the inner crystalline oxide layer.

We found the presence of amorphous oxide in the crystalline layer of the anodic oxide film formed on the Zr–10 at.% Si alloy [15]. Thus, it is also likely that an amorphous oxide is present in the inner crystalline layer on the present Zr–Al alloys. In this case, the cations of Al^{3+} and Zr^{4+} ions can migrate outwards to form an amorphous layer at the film/electrolyte interface. The fraction of amorphous oxide in the inner layer may increase with aluminum content, leading to the thicker outer amorphous layer. A slight reduction of ε_{ox} value by increasing aluminum content from 10 to 16 at.% may be due to increased fraction of the amorphous oxide in the anodic oxide films.

When the aluminum content is increased to 26 at.%, the anodic oxide film becomes amorphous throughout the film thickness (Fig. 4). The amorphous oxide film should be formed both at the alloy/film and film/electrolyte interfaces by cooperative counter migrations of cations and anions. Both aluminum and zirconium are present throughout the film thickness, due to similar migration rates of Al^{3+} and Zr^{4+} ions in growing amorphous oxide [25]. There is a good correlation between the relative migration rates of cations and their single metal–oxygen bond energy [22, 26]. Similar migration rates of Al^{3+} and Zr^{4+} ions arise from their similar metal–oxygen bond strengths (Al^{3+}–O, 280 kJ mol^{-1}; Zr^{4+}–O, 276 kJ mol^{-1}). The GDOES depth profile of the anodic film discloses the incorporation of the boron species from electrolyte. Assuming a constant sputtering rate throughout the film thickness, the boron species are present in the outer 18% of the film thickness. The transport number of cations in anodic Al_2O_3 is 0.4 [27, 28] and that in amorphous anodic ZrO_2 has been predicted to be 0.15 [9]. Assuming linear change in the transport number of cations with alloy composition [7], the transport number of cations of 0.21 is predicted for the anodic film on the Zr–26 at.% Al alloy. Thus, the boron species are present in the major part of the anodic oxide film formed at the film/electrolyte interface, suggesting immobility or slower migration, if any, of boron species in growing anodic oxide on the Zr–26 at.% Al alloy.

Conclusions

Through the examination of structure and dielectric properties of anodic oxide films formed on the sputter-deposited Zr–Al alloys with various compositions, following conclusions are drawn.

1. Crystalline anodic oxide films with a thin amorphous outer layer are formed on the Zr–5, 11, and 16 at.% Al alloys. The anodic oxide film formed on zirconium consists of a mixture of monoclinic ZrO_2 and tetragonal ZrO_2, but the latter phase becomes more predominant with increasing aluminum content in the alloy. Only the tetragonal phase ZrO_2 is detected in the anodic oxide films on the Zr–11 and 16 at.% Al alloys. When aluminum content in the alloy increased to 26 at.%, the anodic oxide film becomes amorphous.

2. Capacitances of the anodic oxide films are enhanced by addition of aluminum, with the maximum value obtained when 11 at.% of aluminum is added. The capacitance of the anodic oxide film formed on Zr–11 at.% Al alloy is 1.7 times than on zirconium at 100 V. The enhanced capacitance is attributed to the increased relative permittivity, which results from the phase transformation from monoclinic to tetragonal by the addition of aluminum.

References

1. Pringle JPS (1980) Electrochim Acta 25:1423–1437
2. Young L, Smith DJ (1979) J ElectrochemSoc 126:765–768
3. Mott NF (1987) Phil Mag B 55:117–129
4. Aladjem A (1973) J Mater Sci 8:688–704
5. Dyer CK, Leach JSL (1978) J Electrochem Soc 125:1032–1042
6. Habazaki H, Uozumi M, Konno H, Shimizu K, Skeldon P, Thompson GE (2003) Corros Sci 45:2063–2073
7. Habazaki H, Shimizu K, Skeldon P, Thompson GE, Wood GC (1997) Proc R Soc Lond A 453:1593–1609
8. Habazaki H, Skeldon P, Thompson GE, Wood GC, Shimizu K (1996) Phil Mag B 73:297–308
9. Habazaki H, Uozumi M, Konno H, Shimizu K, Nagata S, Asami K, Matsumoto K, Takayama K, Oda Y, Skeldon P, Thompson GE (2003) Electrochim Acta 48:3257–3266
10. Habazaki H, Uozumi M, Konno H, Shimizu K, Nagata S, Takayama K, Oda Y, Skeldon P, Thompson GE (2005) J Electrochem Soc 152:B263–B270
11. Habazaki H, Shimizu K, Nagata S, Asami K, Takayama K, Oda Y, Skeldon P, Thompson GE (2005) Thin Solid Films 479:144–151
12. Koyama S, Aoki Y, Nagata S, Kimura H, Habazaki H (2010) Electrochim Acta 55:3144–3151
13. Wang T, Jin ZP, Zhao JC (2001) J Phase Equilib 22:544–551
14. Hashimoto K, Park PY, Kim JH, Yoshioka H, Mitsui H, Akiyama E, Habazaki H, Kawashima A, Asami K, Grzesik Z, Mrowec S (1995) Mater Sci Eng A 198:1–10
15. Koyama S, Aoki Y, Sakaguchi N, Nagata S, Habazaki H (2010) J Electrochem Soc 157:C444–C451
16. Patrito EM, Torresi RM, Leiva EPM, Macagno VA (1990) J Electrochem Soc 137:524–530
17. Zhao XY, Vanderbilt D (2002) Phys Rev B 65:075105
18. Chen Y, Sellar JR (1996) Solid State Ionics 86–8:207–211
19. Lanagan MT, Yamamoto JK, Bhalla A, Sankar SG (1989) Mater Lett 7:437–440
20. Wood GC, Skeldon P, Thompson GE, Shimizu K (1996) J Electrochem Soc 143:74–83
21. Habazaki H, Shimizu K, Nagata S, Skeldon P, Thompson GE, Wood GC (2002) Corros Sci 44:1047–1055
22. Habazaki H, Shimizu K, Nagata S, Skeldon P, Thompson GE, Wood GC (2002) J Electrochem Soc 149:B70–B74
23. Habazaki H, Matsuo T, Konno H, Shimizu K, Nagata S, Matsumoto K, Takayama K, Oda Y, Skeldon P, Thompson GE (2003) Electrochim Acta 48:3519–3526
24. Shimizu K, Kobayashi K, Thompson GE, Skeldon P, Wood GC (1996) Philos Mag B 73:461–485
25. Habazaki H, Skeldon P, Shimizu K, Thompson GE, Wood GC (1995) J Phys D Appl Phys 28:2612–2618
26. Shimizu K, Kobayashi K (1995) J Suf Finish Soc Jpn 46:402–409
27. Shimizu K, Thompson GE, Wood GC, Xu Y (1982) Thin Solid Films 88:255–262
28. Brown F, Mackintosh WD (1973) J Electrochem Soc 120:1096–1102